Assessment of behavioural modification techniques through immersed boundary method simulation of binary particle interactions in isotropic turbulence

L. F. Mortimer [a)] and M. Fairweather

School of Chemical and Process Engineering, University of Leeds, Leeds, LS2 9JT, UK

[a)] *Corresponding author: l.f.mortimer@leeds.ac.uk*

Behavioural modification effects for particle-laden turbulent flows are developed and assessed through high-fidelity modelling using an implementation of the mirroring ghost-cell based immersed boundary method in conjunction with direct numerical simulation. The continuous phase uses the open-source spectral element method-based solver, Nek5000. A dynamic form of the mirroring immersed boundary method is described which also solves for interparticle attraction and repulsion forces allowing for nontrivial collision outcomes such as agglomeration. The solid-phase solver is validated against empirical drag coefficient data as well as spherical bouncing experiments with excellent agreement obtained at low particle Reynolds numbers. Periodic boxes of homogeneous isotropic turbulence are generated using the linear forcing method at $Re_\lambda = 29, 51$ and 120. Ensembles of structure-resolved binary particle collisions are then studied within these boxes, considering the variation of six key mechanical and chemical parameters. These are the coefficient of restitution, Hamaker constant, surface charge potential, inverse Debye length, temperature and Reynolds number. It is established that the coefficient of restitution, inverse Debye length and Reynolds number have the greatest impact on the resulting particle motion and interaction by considering probability density functions of intersurfacial distance and relative particle velocities. Suggestions for real-world procedures which modify these parameters in order to either encourage or discourage particle interaction and potential agglomeration are discussed.

NOMENCLATURE

ACRONYM	DEFINITION
DLVO	Derjaguin and Landau,Verwey and Overbeek
DNS	Direct numerical simulation
GLL	Gauss-Lobatto-Legendre
IB	Immersed boundary
IBM	Immersed boundaries method
LPT	Lagrangian particle tracking
PDF	Probability density function
SEM	Spectral element method

SYMBOL	DEFINITION
Θ	Reduced surface potential
θ	Second Euler angle
κ	Inverse Debye screening length
λ	Taylor microscale
μ_F	Fluid dynamic viscosity
ν_F	Fluid kinematic viscosity

ρ_F	Fluid density
$\boldsymbol{\tau}$	Deviatoric stress tensor
$\boldsymbol{\tau}_f$	Deviatoric stress tensor interpolated onto face
ϕ	First Euler angle
ψ	Third Euler angle
$\boldsymbol{\omega}_P$	Angular velocity vector of particle
$\boldsymbol{A}$	Orientation matrix
A_{LF}	Linear forcing parameter
A	Hamaker constant
A_f	Surface area of face
C_D	Drag coefficient
d_p	Particle diameter
dt	Simulation timestep
dv	Relative particle velocity
dx	Relative separation distance
e_N	Normal coefficient of restitution
$\boldsymbol{f}_{LF}$	Linear forcing source term
$\boldsymbol{F}_{1,2}^{DLVO}$	Interparticle total DLVO force
$\boldsymbol{F}_{1,2}^{VDV}$	Interparticle total van der Waals force
$\boldsymbol{F}_{1,2}^{EDL}$	Interparticle total electric double layer force
$\boldsymbol{F}_P$	Pressure force on IB
$\boldsymbol{F}_T$	Total hydrodynamic translational force on IB
$\boldsymbol{F}_V$	Viscous force on IB
f	IB mesh face identifier
$H_{1,2}$	Inter-surface particle distance
I	Moment of inertia
k_B	Boltzmann's constant
N	Spectral element method order
N_f	Total number of faces
$\boldsymbol{n}_f$	Unit vector normal to face
n	Number density of electrolyte ions
m_p	Mass of particle
p_F	Fluid pressure
p_f	Fluid pressure interpolated onto face
$\boldsymbol{Q}$	Quaternion vector
q_i	Quaternion component i
$\boldsymbol{r}_F$	Centre-face particle distance vector
r_P	Particle radius
Re_τ	Shear / friction Reynolds number
Re_P	Particle Reynolds number
Re_λ	Taylor microscale Reynolds number
t	Time
$\boldsymbol{T}_V$	Total torque on IB
T_F	Fluid temperature
U_∞	Free stream velocity
$\boldsymbol{u}_E$	Fluid velocity at exterior node
$\boldsymbol{u}_F$	Instantaneous fluid velocity
$\boldsymbol{u'}_F$	Instantaneous fluid velocity fluctuation
$\overline{\boldsymbol{u}}_F$	Timewise mean fluid velocity
$\boldsymbol{u}_G$	Fluid velocity at ghost node
$\boldsymbol{u}_{IB}$	Instantaneous velocity of IB surface point
$\boldsymbol{u}_P$	Instantaneous particle velocity
u_r^*	Particle collision relative velocity
u_θ	Collision angle
u'_{RMS}	Root mean square of velocity fluctuation
$\boldsymbol{x}$	Position vector in fluid domain
y^+	Wall distance

I. INTRODUCTION

Particle-laden turbulent flows are ubiquitous in both nature and industry, with most multiphase flows composed of solid-gas or solid-liquid phases. Accurate prediction of multiphase flows is of increasing importance to the understanding of many diverse processes such as drug targeting in blood flows (Zhang et al., 2020), airborne viral droplet dispersion (Dbouk and Drikakis, 2020) and hydrodynamic chemical mixing (Nieto and Gimeno, 2019), to name but a few. In such systems, the ability to predict complex particle-fluid and particle-particle interaction dynamics relies on an understanding of fundamental micro-scale mechanisms. For instance, and of relevance to this work, decontamination of legacy nuclear waste stored in ponds, silos and tanks is of great importance and stands as a matter of increasing urgency throughout the nuclear industry, with UK government recognising decommissioning of legacy nuclear facilities as a national priority. In facilities around the UK and elsewhere, waste suspension flows transport solid-liquid mixtures of legacy material from historic ponds and silos to other interim locations where they are safely stored (WMSYM, 2016). However, at present these processes are performed sub-optimally and with caution due to a lack of understanding of the flow behaviour of the mixtures in question. In practice, the bulk transportive behaviour of interest associated with such activities is often sensitive to many of the material properties and flow conditions. The ability to control mechanical and chemical conditions of the system can be obtained through various means. Firstly, the injection of additives such salt, nanoparticles and polymers (Lumley, 1973) has been shown, even with extremely low concentrations, to have great impact on the continuous phase turbulence properties (Wei and Willmarth, 1992). Furthermore, ambient properties can be modified, such as temperature which can be manipulated through heating or cooling, offering consequences for both the fluid and particle interaction dynamics (Rousta and Lessani, 2020). This sensitivity is hence capable of being exploited, and the variation of such quantities to obtain a desired outcome is referred to as behavioural modification. For instance, this could be used to control the extent of long-term particle migration and interaction events in wall-bounded flows such as particle dispersion, agglomeration and deposition. These processes are of great importance to nuclear waste management and the build-up of corrosion products in reactor fuel assembly coolant flows, as undesirable behaviour such as blockages entails high risks (Wang et al., 2020). That said, it is extremely difficult to probe the effects of such variations experimentally.

Computer simulations offer a means to overcome this difficulty by providing the capability to specify and explore the impact of a set of precise system parameters. The accuracy and reliability of such calculations is based upon both the order of the discretisation techniques used for each phase, as well as the fidelity of the models used to predict the wide array of interactions between the phases. In recent decades the former has been developed to the point that, given sufficient

computational resources, even the smallest flow structures present in turbulent flows are capable of being resolved (Vreman, 2016). This is most often referred to as direct numerical simulation (DNS) and has been used extensively in recent years to develop knowledge surrounding the fundamental dynamics associated turbulent flows (Hussain et al., 1987; Pope, 2001; Piomelli et al., 1988). Considering the latter, precisely modelling micron-scale particle-fluid and particle-particle interactions has long been challenging. In most cases, we have been forced to make assumptions surrounding the particulate or droplet phase such as perfect sphericity, elastic interactions and zero-porosity agglomeration (Maxey and Riley, 1983; Maxey, 1987) . This can lead to inaccuracies in the final predicted bulk behaviour which can generate surprising discrepancies when compared to reproduced experimental flows. Whilst the combination of DNS and Lagrangian particle tracking (LPT) of the particle phase has been used frequently in the last few decades, this approach is more suited to large ensembles of particles ($N_P > 10^6$), with N_P the total number of computational particles contained within the system. Despite these assumptions, LPT has proven a useful tool to explore macroscopic behaviour such as dispersion (Fairweather and Yao, 2009; Crowe et al., 1985; Elghobashi and Truesdell, 2006; Mortimer et al., 2019; Zhao et al., 2012), deposition (Li and Ahmadi, 1992; Li et al., 2013; Walters and Luke, 2010; Soldati and Marchioli, 2009; Winkler et al., 2006) and particle-fluid coupling (Kasbaoui et al., 2019; Monchaux and Dejoan, 2017; Mortimer and Fairweather, 2020; Eaton, 2009; Balachandar and Eaton, 2010). A recent review performed by M. Kuerten (2016) identified the important findings and conclusions obtained over the last few decades surrounding LPT studies, considering the important emergent behaviours in wall-bounded turbulent particle-laden flows such as turbophoresis and preferential concentration (Fessler et al., 1994; Eaton and Fessler, 1994). For increased levels of interaction such as interparticle collisions and agglomeration, further assumptions are introduced into LPT models (Sungkorn and Derksen, 2012). To remove these assumptions and obtain more accurate results, one must develop models which successfully predict the dynamics of more complex particle shapes and interactions. With modern computing, we are now at a stage where the fundamental high-fidelity calculation of small ensembles of these interactions is feasible. In recent years, advances in both computational techniques and power now allow for realistic simulations at high accuracy levels. This provides a suitable framework to investigate and generate understanding of multiphase flows at a more fundamental level and has therefore been of great interest in recent work, in which multiphase computational fluid dynamics is used to obtain insight into such behaviour. In order to constitute a true DNS, the full Navier-Stokes equations must be solved for at all relevant length and time scales, which includes those corresponding to the boundary layer between the bulk fluid and the particle surface, in the case of particle-laden systems. Implicit to this methodology is the simulation of the wake behind the particle, and all inherent hydrodynamic forces on the particle are calculated by integrating the pressure and viscous terms over the structure. Various attempts at constructing such computational methods and algorithms have been carried out in recent years, each offering their own trade-off between accuracy and complexity.

For dynamic particle simulation, it is unfeasible in terms of computational expense to regenerate the computational grid surrounding the particle at each timestep in order to ensure grid points reside perfectly on the surface of the particle. That said, similar approaches such as the conformal arbitrary Lagrangian-Eulerian method have been used previously (Hu, 1996; Hu et al., 2001), with convincing accuracy obtained. In most cases, a permanent Cartesian grid is used to simulate the continuous phase, within which the particle or solid-phase mesh is bound. This solution to the fluid-structure interaction problem wherein Eulerian and Lagrangian coordinates are used for the fluid and structure motion respectively is commonly referred to as the immersed boundary (IB) method and has been widely used in recent years (Kim and Choi, 2019). To account for the coupling between the IB structure and the fluid, momentum forcing is imposed in the Eulerian phase. In all such techniques, two boundary conditions must be satisfied. The first is the no-slip condition on the boundary, which requires that the velocity of the Lagrangian point on the IB is equivalent to the fluid velocity at that location. The second is that the integration of the Cauchy stress tensors across the IB are equivalent for both the structure and fluid phases. The method by which these are imposed determines the general form and accuracy of the IB technique. In the original formulation (Peskin, 2002; Peskin, 1977), the IB is assumed to be composed of massless Lagrangian mesh points, interconnected with springs, with forces (based on Hooke's law) applied back to the Eulerian phase using a distribution function, which tends to blur the representation of the boundary and is only first-order accurate. Various attempts were made in subsequent years to improve the accuracy of this technique, including ensuring the flow is brought to rest on the surface of the stationary boundary via external forcing (Goldstein et al., 1993), however constraints on the upper limit of timesteps were then introduced, leading to increased computational resources required to perform such calculations. Similar attempts at improving this method were performed by (Silva et al., 2007), who used physical arguments to justify the inclusion of the forcing terms. Kim and Peskin (2007) used a variant of the feedback method wherein both massless and massive boundaries were tracked, with the displacements between these boundaries used to calculate the momentum forcing.

Alternatively, rather than using a distributive forcing method to satisfy the boundary conditions, the no-slip boundary condition can be enforced directly on the Lagrangian points of the surface of the IB (Mohd-Yusof, 1997). To achieve this, it is ensured that the velocity field varies smoothly across the sharp interface between the continuous and solid phases by applying an explicit momentum force to the interior boundary Eulerian nodes. This method avoids severe timestep restrictions, and has been used widely in recent years (Uhlmann, 2005; Yang and Balaras, 2006; Luo et al., 2010). However, in the case of dynamic solid phases, local force oscillations were observed leading to wiggles in the solution as the interface was advected, a problem which diminished with reducing grid spacing or timestep. This was also alleviated somewhat by adopting a feedback-based approach where momentum forcing is calculated through the Navier-Stokes equations, using the interpolated fluid/structure

velocities (Uhlmann, 2005). These techniques can suffer from unrealistic mass fluxes across the boundary due to the reversing of the velocity field inside the IB. The ghost-cell based IB method (Tseng and Ferziger, 2003) ensures the correct velocity at the no-slip boundary by extrapolating the fluid flow through a triangle mesh face to a point on the interior of the solid structure. This leads to second-order accuracy and, with some modifications, has shown good promise in the last few decades (Mark and van Wachem, 2008). The mirroring immersed boundary method in particular exhibits convincing behaviour for interacting particles in simple flows (Zastawny et al., 2010; Chi et al., 2017). In this case, the velocity of interior points on the IB are mirrored across the closest triangular face such that interpolation of the velocity at the surface satisfies the Dirichlet condition.

Investigation of microscale particle-fluid behaviours using particle-resolving techniques has already shown much promise, providing insight on many fundamental dynamics. Turbulence modulation effects in decaying isotropic turbulence were investigated by Lucci et al. (2010), generating understanding surrounding how particles influence the development of turbulence kinetic energy and its dissipation rate. Channels with obstacles have also been simulated with a focus on particle collision and adhesion effects (Hosaka et al., 2018). In recent years, fully resolved interparticle collisions have been of great interest, since most solid-fluid flows in nature and industry tend to be of high volume fraction. Zhang et al. (2015) studied collisions in ducts using DNS and Mizuno et al. (2018) considered the effect of the particle wake on the resultant collision distributions. A soft sphere collision model for fully resolved simulations including finite-size particles was developed by Costa et al. (2015) which accounts for both long and short range hydrodynamic interactions, and was applied in Ardekani et al. (2016) who studied sedimentation of spheroidal particles, and in Li et al. (2020) who studied Lagrangian particles in Couette flow. More recently, the hard-sphere model has been applied by Jain et al. (2019) who studied interacting structure-resolved ellipsoids in viscous fluids. The types of collisions considered were more realistic than alternative approaches since associated timescales were more comparable to those used to resolve the fluid. Furthermore, there were no numerical parameters that needed modification which would have detracted from the realism of the simulations. A drawback, however, is that this approach is limited to binary particle interactions, with the collision of three or more particles potentially leading to inaccuracies or otherwise requiring special treatment. In studying granular flow, Buist et al. (2016) used a hybrid approach, with soft-sphere collisions for any interaction with three or greater constituents, and hard-sphere collisions otherwise.

The present work uses the mirroring ghost-cell based immersed boundary method coupled to a spectral element method (SEM) based DNS solver in order to resolve fully the turbulence field around dynamic spherical particle meshes. The aim is to use this technique to study the effect varying several chemical and mechanical properties has on the resulting particle collision, and the potential for particle agglomeration. Collision events are based on those frequently occurring at various locations in a $Re_\tau = 180$ channel flow, with properties chosen to match those of calcite in water, the former being a simulant often used in

flows to represent nuclear waste material. DLVO theory (Derjaguin and Landau, 1941; Verwey and Overbeek, 1955) is used to calculate the interaction potential of charged particle surfaces within the liquid medium, allowing for implicit agglomeration eventualities upon collision. DLVO theory interparticle forces cover several important parameters. Attraction is modulated by the Hamaker constant, which measures the strength of van der Waals forces between particles. Repulsion is modulated by the electrostatics involved with diffused electrical double layers which overlap when particles move very close to one another, generating a separating force. The extent of this layer is measured as the Debye length. The variation of system parameters such as Hamaker constant, temperature, Reynolds number, collision coefficient of restitution and electric double layer properties such as Debye length on bulk flow observables is used to provide insight into means of behavioural modification. The generation of this fundamental understanding is attractive in many industries since simple changes to the flow properties via heating or some other flow additive in order to obtain a desired behaviour is much more efficient and resourceful than redesigning the processing system.

II. Methodology

A. Linearly forced homogeneous isotropic turbulence

The simulations presented in this article all take place in periodic boxes of linearly forced homogeneous isotropic turbulence. The continuous phase dynamics for the flow in which the particles are immersed are governed by the incompressible Navier-Stokes equations. These are solved using the spectral-element method-based DNS solver, Nek5000 (Fischer et al., 2008). The flow equations are:

$$\boldsymbol{\nabla} \cdot \boldsymbol{u}_F = 0, \tag{1}$$

$$\frac{\partial \boldsymbol{u}_F}{\partial t} + \boldsymbol{u}_F \cdot \boldsymbol{\nabla} \boldsymbol{u}_F = -\frac{\boldsymbol{\nabla} p_F}{\rho_F} + \frac{1}{\rho_F} \boldsymbol{\nabla} \cdot \boldsymbol{\tau} + \boldsymbol{f}_{LF}. \tag{2}$$

Here, $\boldsymbol{u}_F(\boldsymbol{x}, t)$ is the fluid velocity vector at Cartesian position vector $\boldsymbol{x}$, t is the time, p_F is the fluid pressure, ρ_F is the fluid phase density, and $\boldsymbol{\tau}$ is the deviatoric stress tensor for a Newtonian fluid. The acceleration, $\boldsymbol{f}_{LF}$, is a linear forcing source term (Rosales and Meneveau, 2005; Lundgren, 2003), given by $\boldsymbol{f}_{LF} = A_{LF} \boldsymbol{u'}_F$, where $\boldsymbol{u'}_F(\boldsymbol{x}, t)$ is the instantaneous velocity fluctuation $\boldsymbol{u'}_F = \boldsymbol{u}_F - \overline{\boldsymbol{u}}_F$, and $\overline{\boldsymbol{u}}_F(\boldsymbol{x}, t)$ is the timewise mean velocity. The parameter A_{LF} relates to a user-supplied eddy turnover time scale, and tuning of this parameter allows one to obtain a desired Reynolds number (based on the Taylor microscale, λ), for a given fluid kinematic viscosity, ν_F. Despite relatively long times to a statistically stationary state when compared to other methods, this technique was chosen due to its lack of computational complexity (Janin et al., 2021). This is applied to all fluid nodes in the continuous phase. Due to the very low volume fraction of particles used within this study, particle-fluid coupling effects arising from the presence of moving particles which may interfere with the nature of this forcing technique are negligible. That said, particle-scale turbulence modulation is captured in the immersed boundary method.

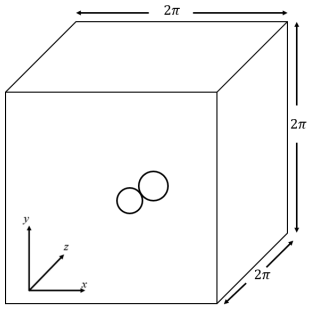

Figure 1: Schematic of the computational domain for the continuous phase containing a single binary particle interaction event occurring in homogeneous isotropic turbulence.

The computational mesh within which Eqns. (1) and (2) are solved consists of a box with length 2π in each direction, which is discretized into 48×48×48 equally distributed cubic spectral elements of order $N = 7$. The boundary conditions enforced at the extent of the axes passing though the centre of the domain $(-\pi, \pi)$ are periodic. The domain for the continuous phase is illustrated in Figure 1. More details surrounding the single-phase solver may be found in Mortimer et al. (2019).

B. Ghost-cell based mirroring immersed boundary method

In order to represent an arbitrary finite-sized particle of any convex topology, subject to a flow field, a ghost-cell based mirroring immersed boundary method has been developed to compute motion and feedback concurrently with the fluid-phase solver Nek5000. The original IB method concept is detailed in Peskin (2002) wherein the structure is reconstructed within the continuous phase as a boundary which is coupled to the flow field via forcing. To achieve this, momentum transfer conditions are imposed on the surface of the boundary through an additional delta function term added to the Navier-Stokes equations, in an effort to satisfy the no-slip requirement. It is possible to extend this idea to a rigid boundary by reducing the deformability of the elastic fibres forming the structure, and it is suggested by previous authors (Beyer and LeVeque, 1992) that discrete forcing (as opposed to continuous forcing) approaches are easier to implement and also obtain good accuracy when considering arbitrary and rigid particle species. The method implemented in this work is based on the second-order accurate 'mirroring IB' specification developed by Mark and van Wachem (2008).

Building upon Eqns. (1) and (2), the first immersed boundary condition requires that $\boldsymbol{u}_F = \boldsymbol{u}_{IB}$ everywhere on the surface of the IB, where $\boldsymbol{u}_{IB}$ is the instantaneous velocity of the surface point. Note that this is not necessarily equivalent to the translational velocity of the IB structure due to the possibility of angular velocity. This requirement ensures that the velocity of the connected fluid satisfies the no-slip condition. The solver reads in a standard format triangle mesh three-dimensional object file containing a structured surface grid corresponding to a particle which consists of vertices and faces, which forms the topology of the IB. For all simulations performed in this work, a computational icosphere mesh is used to represent spherical particles, which is stored in the face-vertex representation and consists of 320 faces. The particle icosphere mesh discretization was chosen to be the most refined representation of a sphere where the triangular spacing was still on the order of the fluid computational GLL point spacing. Studying the effect of subdividing once more to get the next most resolved icosphere (1280 faces), we found that the improvement to the drag coefficient was negligible. An example of this discretization is presented in Figure 2. Each face has an associated centroid position and velocity, where the velocity is derived from the global particle angular velocity. The no-slip condition is then such that $\boldsymbol{u}_F = \boldsymbol{u}_{IB} = \boldsymbol{u}_P + \boldsymbol{\omega}_P \times \boldsymbol{r}_f$ on each particle face, f. Here, $\boldsymbol{u}_P$ is the particle translational velocity, $\boldsymbol{\omega}_P$ is the angular velocity of the particle and $\boldsymbol{r}_F$ is the position vector from the centre of the particle, a distance r_P to the centroid of face f.

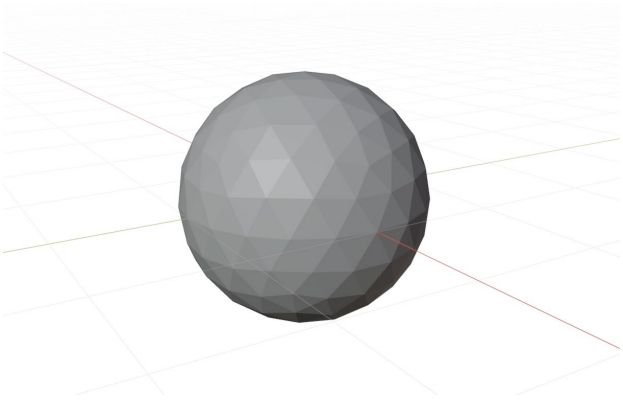

Figure 2: Computational icosphere mesh consisting of 320 equilateral triangular faces representing IB for spherical particle.

The 'mirroring' implementation to ensure the no-slip requirement is carried out by first assigning each cell (formed by the bisectors between two neighbouring Gauss-Lobatto-Legendre (GLL) points) in the continuous phase solver a label. These are exterior nodes (E) which reside outside the boundaries of the IB; ghost nodes (G) which are nodes inside the boundary but are adjacent to exterior nodes; and finally interior nodes (I), which are inside the IB but not adjacent to any exterior nodes. These assignments are illustrated in Figure 3. Indicated in the diagram, the velocity at the ghost node is modified such that linear interpolation at the midpoint of the line connecting it with the mirrored node in the continuous phase domain would yield exactly the velocity of that particular surface of the IB. The velocity at the exterior node is determined using spectral interpolation, exploiting the function-based nature of the SEM. Due to symmetry, the interior node velocity is then calculated using:

$$\boldsymbol{u}_G = 2\boldsymbol{u}_{IB} - \boldsymbol{u}_E. \tag{3}$$

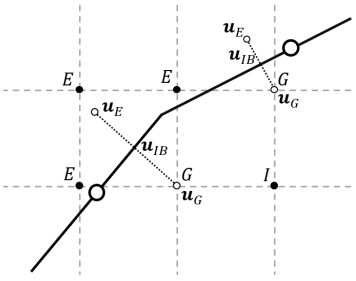

Figure 3: Two-dimensional representation of computational domain containing part of an immersed boundary. Dashed lines meet at continuous phase GLL points. Large circles represent the midpoints of IB triangle faces. Each small circle represents a node with labels: E – exterior node; G – ghost node; I – interior node. Dotted lines demonstrate the mirroring of the ghost node velocity across an IB surface onto an interpolated point in the exterior fluid.

The exact point of mirroring is determined by calculating the shortest distance between the interior ghost node and the closest triangular planar surface. The position of the exterior point at which the velocity is then interpolated is subsequently calculated by reflecting the ghost node across the surface. All other interior velocities are set to be equivalent to the velocity of their closest boundary.

C. Calculation of hydrodynamic forces and torques on surface of IB

To advect and rotate the particle, forces and torques due to pressure and viscous contributions are calculated using interpolations of the local fluid pressure and viscous stress tensor. The equation for the total hydrodynamic force exerted on an IB (Ouchene, 2020) is:

$$\boldsymbol{F}_T = \int_{IB} (\boldsymbol{F}_P + \boldsymbol{F}_V)\, dS = \int_{IB} (-p_F \boldsymbol{\delta} + \boldsymbol{\tau}) \cdot \boldsymbol{n}\, dS. \tag{4}$$

Here, $\boldsymbol{F}_T$ is the total translational force on the particle, with $\boldsymbol{F}_P$ and $\boldsymbol{F}_V$ the pressure and viscous components, respectively. The two terms in Eqn. (4) can be recast in terms of a summation of forces on each face of the IB as follows:

$$\boldsymbol{F}_P = \sum_{f=1}^{N_f} -p_f \boldsymbol{n}_f A_f. \tag{5}$$

Since the pressure field inside the IB is undefined, two exterior points are used for the interpolation of pressure onto the face, f, with the subscript referring to the current face in the summation, and N_f being the total number of faces in the particle mesh. After interpolation, p_F is the pressure at the face centroid, $\boldsymbol{n}_f$ is a unit vector normal to face f, and A_f is the surface area of the face. The viscous term is calculated as follows:

$$\boldsymbol{F}_V = \sum_{f=1}^{N_f} \boldsymbol{\tau}_f \cdot \boldsymbol{n}_f A_f. \tag{6}$$

Here, the derivatives in the viscous stress tensor, $\boldsymbol{\tau}_f$, are determined by interpolating velocities onto points which are projections of an exterior extrapolation point onto the Cartesian axis. Of course, the velocity at the triangle centroid is known from the IB condition, and hence only three velocities need to be interpolated to obtain all three Cartesian derivatives.

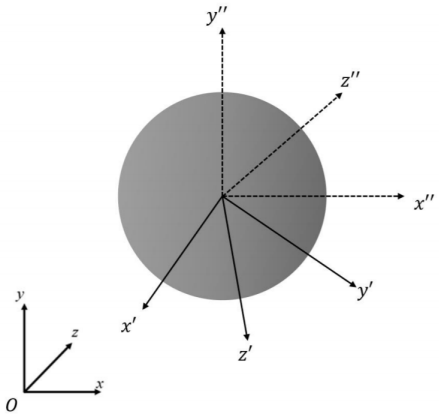

Figure 4: Schematic for rotating particle with co-moving frame (primed) and the particle reference frame (double-primed).

For rotation, particle orientation is dealt with using the quaternion formulation (Zhao et al., 2015). The orientation can be fully defined by three Euler angles, ϕ, θ and ψ which represent the angles between the co-moving frame (primed) and the particle frame (double-primed), as in Figure 4. Following the definition of quaternions (or Euler parameters) as given by Mortensen et al. (2008), it is possible to construct a full orientation state (q_0, q_1, q_2, q_3) using Eqns. (7)-(10):

$$q_0 = \cos\left(\frac{1}{2}(\psi + \phi)\right)\cos\left(\frac{\theta}{2}\right), \tag{7}$$

$$q_1 = \cos\left(\frac{1}{2}(\psi - \phi)\right)\sin\left(\frac{\theta}{2}\right), \tag{8}$$

$$q_2 = \sin\left(\frac{1}{2}(\psi - \phi)\right)\sin\left(\frac{\theta}{2}\right), \tag{9}$$

$$q_3 = \sin\left(\frac{1}{2}(\psi + \phi)\right)\cos\left(\frac{\theta}{2}\right). \tag{10}$$

From these, an orientation matrix, $\boldsymbol{A}$, can be constructed, capable of transforming between the co-moving frame and the particle frame, as in Eqn. (11):

$$\boldsymbol{A} = \begin{pmatrix} 1-2(q_2^2+q_3^2) & 2(q_1q_2+q_0q_3) & 2(q_1q_3-q_0q_2) \\ 2(q_1q_2-q_0q_3) & 1-2(q_1^2+q_3^2) & 2(q_2q_3-q_0q_1) \\ 2(q_1q_3+q_0q_2) & 2(q_2q_3+q_0q_1) & 1-2(q_1^2+q_2^2) \end{pmatrix}. \tag{11}$$

Each timestep the quaternion vector $\boldsymbol{Q} = (q_0, q_1, q_2, q_3)$, and the angular velocity vector (in the particle co-moving reference frame) $\boldsymbol{\omega}_P = \left(\omega_{x'}, \omega_{y'}, \omega_{z'}\right)$, are also tracked. The time-varying quaternion vector differential equation is:

$$\frac{d\boldsymbol{Q}}{dt} = \begin{pmatrix} \frac{dq_0}{dt} \\ \frac{dq_1}{dt} \\ \frac{dq_2}{dt} \\ \frac{dq_3}{dt} \end{pmatrix} = \begin{pmatrix} q_0 & -q_1 & -q_2 & -q_3 \\ q_1 & q_0 & -q_3 & q_2 \\ q_2 & q_3 & q_0 & -q_1 \\ q_3 & -q_2 & q_1 & q_0 \end{pmatrix} \begin{pmatrix} 0 \\ \omega_{x'} \\ \omega_{y'} \\ \omega_{z'} \end{pmatrix}, \tag{12}$$

and the corresponding Eulerian torque equation for the time-varying angular momentum is given by:

$$I \frac{d\boldsymbol{\omega}_P}{dt} = \boldsymbol{T}_V, \tag{13}$$

where I represents the moment of inertia of the rotating particle, and $\boldsymbol{T}_V = \sum_{\boldsymbol{f}} \boldsymbol{r}_f \times \boldsymbol{F}_{V,f}$ represents the total off-normal torque contribution from the viscous force calculation. For spheres, $I = I_{sphere} = \frac{1}{10} m_p d_p^2$, where m_p is the mass of the particle and d_p is the sphere diameter. Due to floating-point precision errors inherent in performing calculations using quaternions, at the end of each timestep, the quaternion vector is normalized by performing the following operation:

$$\boldsymbol{Q}' = \boldsymbol{Q}(q_0^2 + q_1^2 + q_2^2 + q_3^2)^{-\frac{1}{2}}. \tag{14}$$

D. Particle-particle collisions and interactions

Whilst advected by the flow, particles are capable of undergoing various interactions. In this study, we consider the effects of momentum exchange during collisions along with interspherical van der Waals attraction and electric double layer repulsion. Collisions are performed using the inelastic hard-sphere approach (Derksen, 2011), with varying normal coefficients of restitution, e_n. The choice to use this approach as opposed to the soft-sphere mechanism was based on computational efficiency and the sensitivity of the collision model relation to the number of colliding bodies observed in previous work (Buist et al., 2016). Furthermore, we are considering the sensitivity to an adjustable parameter, the coefficient of restitution, which is relatable back to the properties associated with the soft sphere model. In this sense, we are not targeting a specific system but rather considering the variation of energy lost during a collision, so that precisely simulating a specific interaction lies outside the focus of this study. To better represent the type of binary interactions which take place in LPT simulations (which typically only consider normal momentum exchange), the friction coefficient, μ, was set to zero and the tangential momentum exchange vector was neglected. Upon advection, particle pairs are checked for a potential collision event. The sole condition for collision is that their intersurfacial distance, H_{12}, is less than zero, treating the IB structures as perfect spheres. During the timestep over which this occurs, the particles collide inelastically and their resulting translational velocities ($\boldsymbol{u'}_{P,1}, \boldsymbol{u'}_{P,2}$) and positions ($\boldsymbol{x'}_{P,1}, \boldsymbol{x'}_{P,2}$) are evaluated as:

$$\boldsymbol{u}'_{P,1} = \boldsymbol{u}_{P,1} + \frac{m_{P,2}}{m_{P,1} + m_{P,2}}(1 + e_n)\left(\left(\boldsymbol{u}_{P,2} - \boldsymbol{u}_{P,1}\right) \cdot \hat{\boldsymbol{n}}\right)\hat{\boldsymbol{n}}, \tag{15}$$

$$\boldsymbol{u}'_{P,2} = \boldsymbol{u}_{P,2} - \frac{m_{P,1}}{m_{P,1} + m_{P,2}}(1 + e_n)\left(\left(\boldsymbol{u}_{P,2} - \boldsymbol{u}_{P,1}\right) \cdot \hat{\boldsymbol{n}}\right)\hat{\boldsymbol{n}}, \tag{16}$$

$$\boldsymbol{x}'_{P,1} = \boldsymbol{x}_{P,1} + t_{col}\boldsymbol{u}'_{P,1}, \tag{17}$$

$$\boldsymbol{x}'_{P,2} = \boldsymbol{x}_{P,2} + t_{col}\boldsymbol{u}'_{P,2}. \tag{18}$$

In the simulations carried out here, only binary collisions are considered. Furthermore, all collisions are tracked, no matter how frequent, and overlap of the spheres is never permitted nor observed under this approach. Although not used in the present work, particle-wall collisions are handled such that if any vertex in the particle mesh surpasses the boundary, the particle velocity in the direction normal to the wall is reversed, and the particle deflects by the amount it penetrated the barrier. Periodic boundaries, employed below, work in a similar manner, in that as soon as a vertex exceeds the boundary, the particle is reinjected in the appropriate location at the opposite side of the periodic box. This means that the particle can appear to 'jump', but for low particle size with respect to the geometry, the low occurrence of such events means that the error which results from this effect is negligible. Finally, intersurface sphere-sphere DLVO (Derjaguin and Landau, 1941; Verwey and Overbeek, 1955) forces are calculated and included in the particle force balance to account for van der Waals attraction and electric double layer repulsion. The equation for the attraction or repulsion caused by spherical particle, 1, on spherical particle, 2, is as follows:

$$\boldsymbol{F}_{1,2}^{DLVO} = \boldsymbol{F}_{1,2}^{VDV} + \boldsymbol{F}_{1,2}^{EDL}, \tag{19}$$

where $\boldsymbol{F}_{1,2}^{VDV}$ is the van der Waals attractive term and $\boldsymbol{F}_{1,2}^{EDL}$ is the electric double layer term. The van der Waals term, which is of great importance in colloidal chemistry, arises due to the electrostatic attraction induced by London dispersion forces (Stenhammar et al., 2010). The electric double layer term arises due to an interfacial pair of ion layers, the first of which screens the second, which are formed on an object when exposed to a fluid. The surface charge potential is hence reduced as one moves away from the surface. These two forces are given as:

$$\boldsymbol{F}_{kl}^{VDV} = \frac{-Ar_P\hat{\boldsymbol{n}}}{12H_{1,2}^2}, \tag{20}$$

$$\boldsymbol{F}_{kl}^{EDL} = \frac{64\pi r_P n k_B T_F \Theta^2 e^{-\kappa H_{1,2}}}{\kappa}\hat{\boldsymbol{n}}. \tag{21}$$

In the above equations, A is the Hamaker constant, r_P is the particle radius, $H_{1,2}$ is the inter-surface distance between the two spheres, n is the number density of electrolyte ions, k_B is Boltzmann's constant, T_F is the fluid temperature, Θ is the reduced surface potential and κ is the inverse Debye screening length. Finally, $\hat{\boldsymbol{n}}$ is a unit vector pointing along the line joining the centre of particle 1 to particle 2.

III. RESULTS AND DISCUSSION

A. Validation of immersed boundary method

To validate the implementation of the immersed boundary method, and determine accuracy, flow around a sphere was performed at various Reynolds numbers in order to calculate the drag coefficient, C_D. The mesh was equivalent to that detailed in the methodology, with the physical length of the domain this time set to $20m$, in line with Mark and van Wachem (2008). Boundary conditions for this validation flow consisted of constant velocities ($u_F = U_\infty$), where U_∞ is the free stream velocity, on all walls other than the outlet upon which a Neumann boundary condition was used. Equally, the outlet used a constant pressure boundary condition whereas the remaining walls used Neumann pressure conditions. The parameters used in these validation simulations are presented in Table 1, with fluid parameters matching those of Mark and van Wachem (2008). Here, Re_P is the particle Reynolds number, $Re_P = 2U_\infty r_P/\nu_F$, with r_P the sphere radius. Note here that, although unrealistic, the density and viscosity have been chosen to obtain a specific particle Reynolds number. For the range of Reynolds numbers considered, the resulting dynamics are dependent only on the Reynolds number. Sensitivity studies were performed on the time step, dt, with values lower that indicated having a negligible effect on the final calculated drag coefficient. At the start of the simulation, the IB was fixed at the centre of the domain, and although forces were calculated on the particle, the structure was not moving.

Table 1: Parameters for mirroring immersed boundary method validation simulations.

Re_P	U_∞ (ms^{-1})
0.01	0.00025
0.1	0.0025
1	0.025
10	0.25
100	2.5

Constants	
μ_F (Nsm^{-2})	0.01
r_P (m)	0.2
ρ_F (kgm^{-3})	1.0
ν_F (m^2s^{-1})	0.01
dt (s)	0.001

The simulations were performed until the calculation of drag coefficient carried out at each timestep was unchanging. Eqns. (5) and (6) were used to calculate the total force on the IB, which was then converted into a drag coefficient using the following equation (Stokes, 1851):

$$C_D = \frac{F_x}{\frac{1}{2}\rho_F U_\infty^2 \pi r_P^2}. \tag{22}$$

The time evolution of the calculated drag coefficient is presented in the left plot of Figure 5. Clearly in all cases, the simulation converged towards the expected coefficient in less than a second, with minor fluctuations at the start due to the sudden appearance of a particle in an otherwise simple flow. The right plot in Figure 5 compares the converged values (taken at t = 2s)

to those predicted by the frequently used empirical correlation of Schiller and Naumann (1933). Excellent agreement is obtained for particle Reynolds numbers lower than 10, with good agreement obtained at those higher, although in both cases the drag coefficient is slightly underpredicted. This may be due to the imperfections in sphericity associated with the icosphere representation of the particle which may induce further drag-reducing effects. It could also be due to insufficient grid resolution close to the particle to fully capture its wake. That said, high particle Reynolds numbers are unlikely to be observed in binary particle collisions, and the agreement is satisfactory.

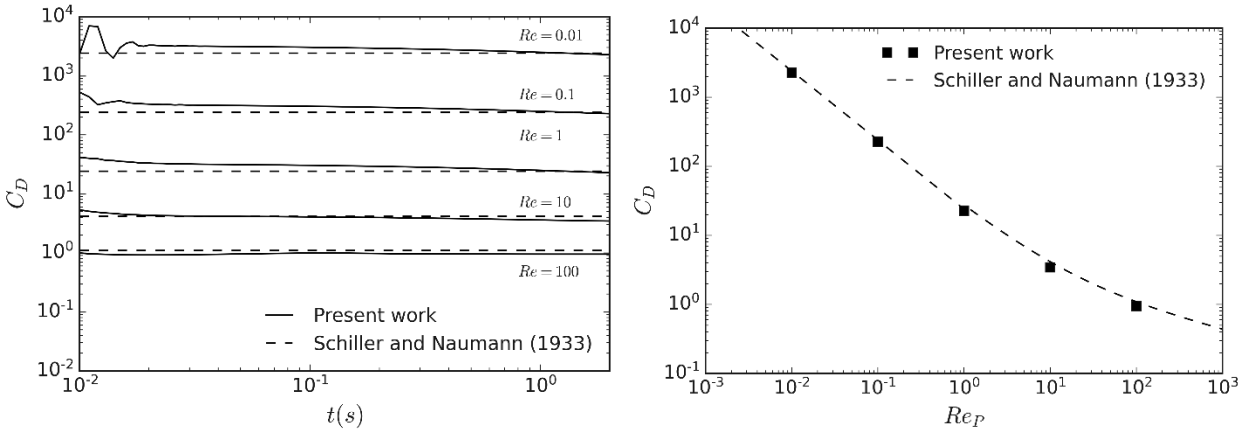

Figure 5: Temporal evolution of calculated drag coefficient from validation simulations compared against empirical relationship.

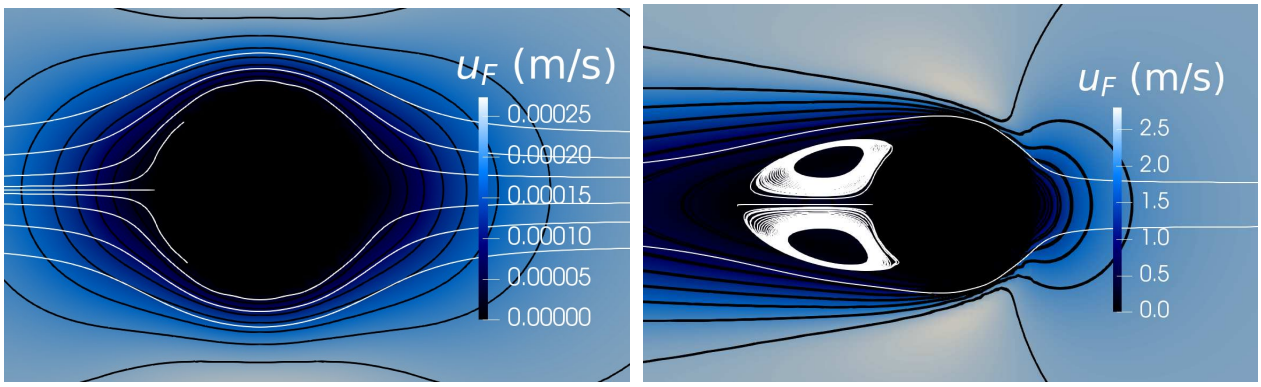

Figure 6: Instantaneous streamwise velocity flow field surrounding stationary IB sphere at $Re_P = 0.01$ (left) and $Re_P = 100$ (right). White lines indicate streamlines, whilst black lines are contours of velocity magnitude (ms^{-1}).

Finally, to demonstrate the flow field surrounding the IB in these validation simulations, a slice of the instantaneous streamwise velocity is illustrated in Figure 6, with the flow being from right to left. Here, coloured lines are contours of velocity magnitude. Both of these snapshots also indicate instantaneous fluid streamlines, which were generated via Runge-Kutta 4th order integration beginning at the minimum boundary in the x-direction and terminating either at the maximum boundary or when the velocity was sufficiently low. Further streamlines were generated within the wake in the $Re_P = 100$ plot using a similar method.

To validate both the translational dynamics and the hard sphere collision mechanism, further simulations were performed of bouncing particles falling within a stagnant vertical domain consisting of $20 \times 80 \times 20$ elements. The extent of the domain was $0m \leq y \leq 0.08m$ in the vertical direction and $-0.01m \leq x, z \leq 0.01m$ in the two transverse directions. In line with the study of Gondret et al. (2002), Teflon ($\rho_P = 2150\ kg\ m^{-3}$) and steel ($\rho_P = 7800\ kg\ m^{-3}$) spheres of radius $0.003m$ and $0.0015m$ were dropped into air ($\rho_F = 1.2\ kg\ m^{-3}, \mu_F = 1.85 \times 10^{-5}\ Nsm^{-2}$) and oil ($\rho_F = 9350\ kg\ m^{-3}, \mu_F = 10^{-3}\ Nsm^{-2}$) respectively. Their initial vertical distances were set equal to those identified as the maxima of the first rebound in each case. Coefficients of restitution were set to 0.8 for Teflon in air and 0.6 for steel in oil, matching those obtained in the experimental collisions with the wall. The constant timestep used for these simulations was $dt = 1 \times 10^{-4}\ s$. The upper and lower extents of the domain were considered walls for the purposes of boundary conditions. Collisions with the wall were handled identically to those with particles.

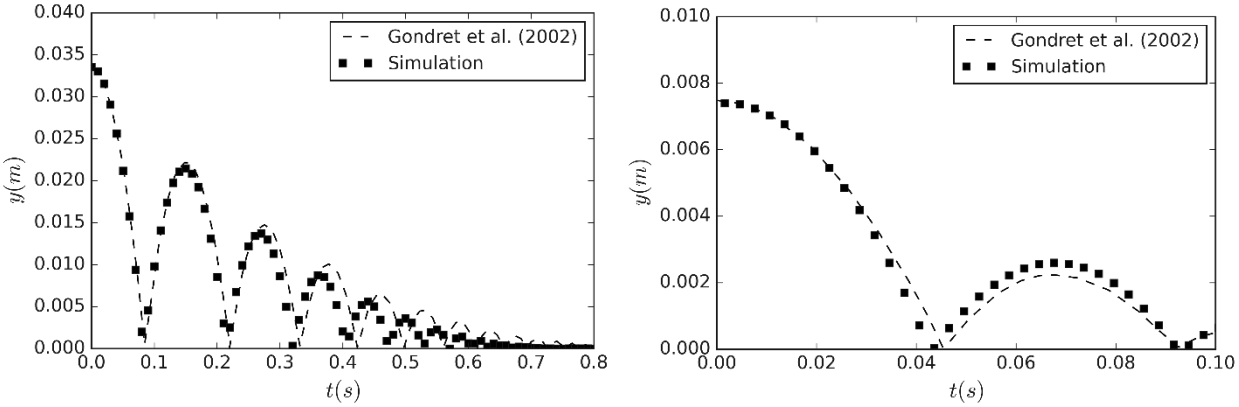

Figure 7: Calculated vertical trajectories of Teflon sphere in air (left) and steel sphere in oil (right) compared to those obtained in the experiments of Gondret et al. (2002).

Figure 7 compares the trajectories calculated during these simulations with those obtained in the corresponding experiments of Gondret et al. (2002). For the Teflon sphere in air, the agreement with the initial bounce trajectory is excellent, with further bounces deviating slightly, a discrepancy which grows over time. This is due to the sensitivity of long term positions to the initial conditions and parameters. Furthermore, in the experiment the coefficient of restitution is not consistently exactly 0.8, but deviates from this slightly with time, leading to unpredictability over long timeframes. Still, the initial bounce trajectories are convincing. For steel in oil, good agreement is also obtained, with the inclusion here of much stronger hydrodynamic fluid forces (due to the increased fluid density) also generating similar trajectories to those obtained in the experiment. Again, the results are very sensitive to initial position and coefficient of restitution.

B. Homogeneous isotropic turbulence

The binary particle interaction simulations studied within this work take place within boxes of homogeneous isotropic turbulence which are generated as detailed in the methodology section. To motivate the selection of Taylor Reynolds numbers, a typical previously studied case of a $Re_\tau = 180$ channel flow is considered (Mortimer and Fairweather, 2020; Mortimer et al., 2019). Here, we choose the Taylor microscale as a characteristic parameter for the turbulence. This is because the scales at which particle-particle and particle-fluid interactions take place are largely isotropic (Oesterle and Petitjean, 1993), hence to study collisions on the interaction-scale, we may consider local regions of turbulence with the same characteristics as those present at various locations across the wall-normal direction of the channel flow. Previously statistically settled single-phase channel flow simulations were continued for calculation of the Taylor microscale (Segalini et al., 2011) according to:

$$\lambda = \sqrt{\frac{u_{RMS}'^2}{\left(\frac{\partial u_{RMS}'}{\partial x}\right)^2}}\ , \tag{23}$$

where u'_{RMS} represents the root-mean-square (RMS) of the fluctuating velocity field. These calculations were then used to generate the variation of Taylor Reynolds number, $Re_\lambda = u_{rms}\lambda/\nu_F$, with wall-distance. These are presented in Figure 8, where length scales are non-dimensionalised using wall units. The left plot demonstrates the variation of the Taylor microscale, which is relatively constant within the bulk flow ($y^+ > 35$), and increases somewhat in the near-wall region. If we consider the derived Taylor Reynolds number on the same scale, however, we see more variation across the half-height of the channel. Based on this distribution, a typical Reynolds number of $Re_\lambda = 51$ representative of the channel flow was chosen as a target for the turbulence characteristic in the homogeneous isotropic box of turbulence. This closely relates to the turbulence level in the region of a channel flow where the agglomeration efficiency is high (Mortimer et al., 2020). To further discern the effect of modification of turbulence level on the resulting binary collision dynamics, two other isotropic boxes were also simulated, targeting $Re_\lambda = 120$ and Re_λ =29. The simulation parameters for all these flows are presented in Table 2.

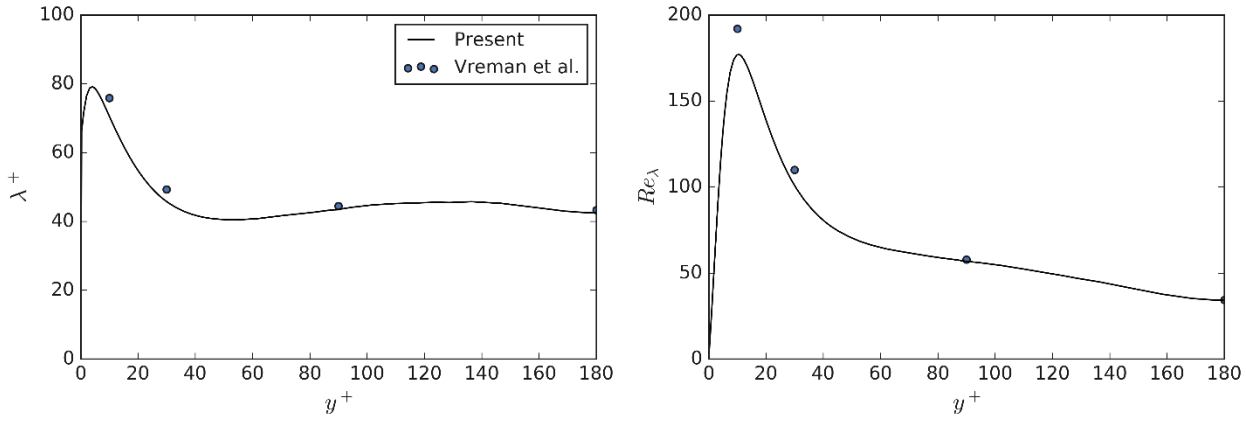

Figure 8: Variation of Taylor microscale in wall units (left) and Taylor Reynolds number (right) with wall distance in DNS of turbulent channel flow at $Re_\tau = 180$. Comparisons are made against the findings of Vreman and Kuerten (2014).

Table 2: Simulation parameters for periodic boxes of homogeneous isotropic turbulence.

Re_λ	A	$\rho_F\ (kgm^{-3})$	$\nu_F\ (m^2s^{-1})$
29	0.0667	1.0	4.491×10^{-3}
51	0.2	1.0	4.491×10^{-3}
120	1.0	1.0	1.272×10^{-2}

Each simulation was initialized using the Arnold-Beltrami-Childress flow (Dombre et al., 1986), an exact solution of the Euler equation with a well-defined initial turbulence energy spectrum. The timestep was modified automatically to ensure a Courant number of lower than 0.5 throughout the entire simulation. Both the global mean and the RMS of velocity fluctuations within each box were monitored to ensure both that a substantial mean did not develop and that the RMS reached a statistically stationary state. The time evolution of these quantities is presented in Figure 9.

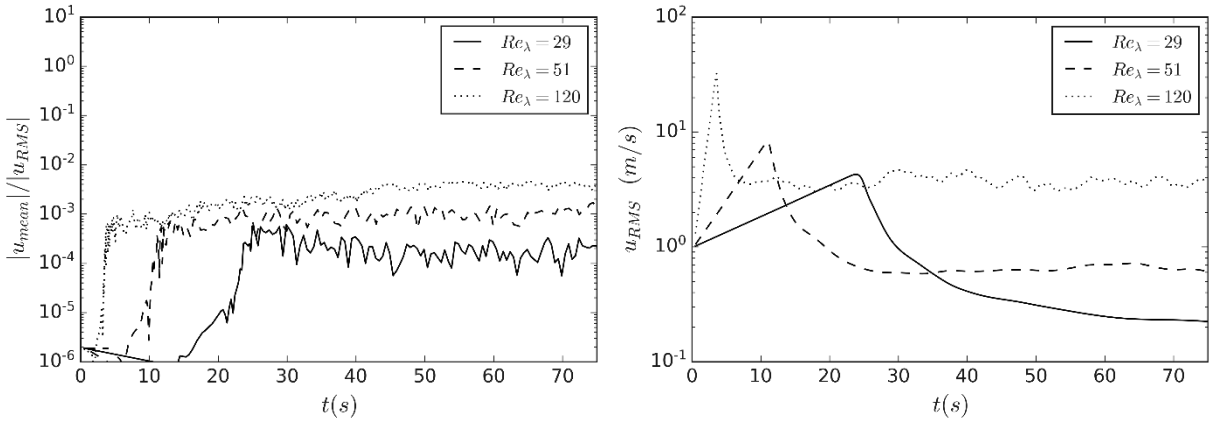

Figure 9: Time evolution of absolute value of mean velocity vector normalized by the root-mean-square of velocity (left) and the root-mean-square of velocity (right) at three different Reynolds numbers based on the Taylor microscale.

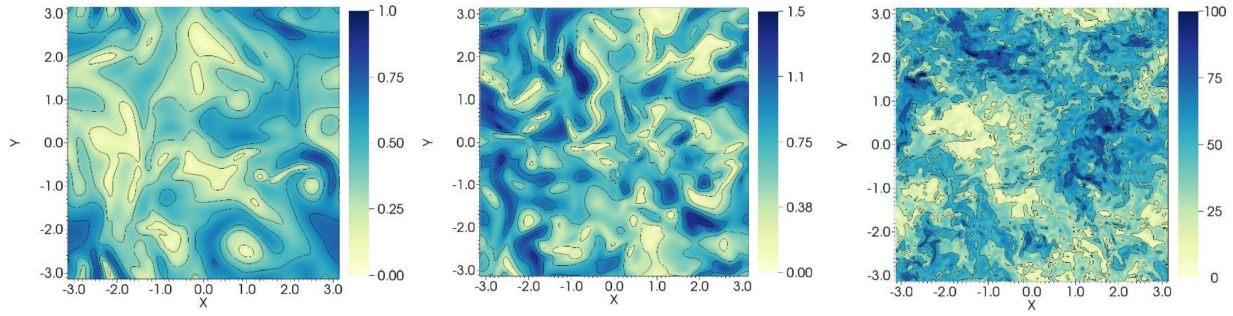

Figure 10: Instantaneous pseudocolour plots of velocity magnitude in the $Re_\lambda = 29$ (left), $Re_\lambda = 51$ (middle), and $Re_\lambda = 120$ (right) homogeneous isotropic boxes.

In each case, the initial transient period involves an increase in turbulence kinetic energy as the dissipation associated with the initial solution is greatly outweighed by the forcing's energy injection. After reaching a critical value of u_{RMS}, each system undergoes a sudden transition into turbulence. The dissipation from thereon works to reduce the kinetic energy of the system until a statistically stationary state is reached where the forcing energy injection and the turbulence energy dissipation are approximately equal. Despite minor fluctuations, the RMS of velocity fluctuations remains effectively stationary after that point. Furthermore, the left plot indicates that the mean velocity remains bounded ($u_{mean} < O(10^{-3})$) in all cases, demonstrating the stability of the method. To illustrate the topology of the turbulence field, contour plots of velocity magnitude are presented in Figure 10.

C. Behavioural modification effects

Having verified the accuracy of the particulate-phase solver as well as having obtained suitable continuous phase initial conditions, this final section considers the interaction within these boxes between two identical spherical particles.

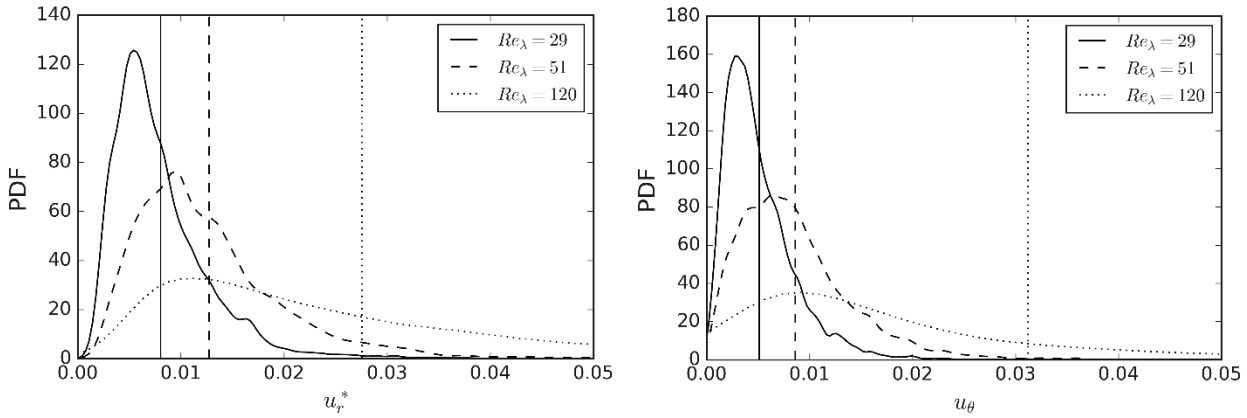

Figure 11: Particle relative collision velocities (left) and collision angles (right) from four-way coupled LPT simulations using calcite particles in $Re_\tau = 180$ channel flow used to determine initial conditions for present IB method simulations. Vertical lines indicate means.

Using the statistically stationary states of homogeneous isotropic turbulence obtained as described in Section III-B, two particles were injected into each box with relative initial velocity vectors matching those most commonly occurring from collision events sampled in the equivalent wall-normal regions of a four-way coupled multi-phase channel flow simulation described in previous work (Mortimer et al., 2020). The injected particles are identical and have radius r_p/D_{BOX} = 0.026 where D_{BOX} is the diameter of the isotropic box mesh. The particle sizes within the domain with respect to the turbulent scales were chosen to ensure at least 10 GLL points reside within the particle mesh across each spatial direction.

In these prior simulations, particle velocity vectors were calculated in a reference frame moving with the local flow mean streamwise velocity. This enables us to approximate particle collisions in a reference frame moving with the fluid downstream inside the channel flow. The relative collision velocity distributions and angles are presented in Figure 11, with vertical lines indicating the mean values chosen as initial conditions for the present work. Here, u_r^* represents the relative particle velocity non-dimensionalized by bulk length and time scales, and u_θ is the angle in radians. In all cases, the collision angles are very low. Since the Stokes number is low for these simulations, the collision angles are almost always indicative of glancing collisions in the fluid reference frame. The global simulation parameters (material and chemical properties) were chosen to represent calcite particles in suspension in water, with other simulations representing deviations to each of several key variables. These are presented in Table 3.

Table 3: Simulation parameters for behavioural modification effects study.

SIM	**0**	**1A**	**1B**	**2A**	**2B**	**3A**	**3B**	**4A**	**4B**	**5A**	**5B**	**6A**	**6B**
e_N	0.4	0.2	0.6	0.2	0.6	0.4	0.4	0.2	0.6	0.2	0.6	0.2	0.6
$A\ (zJ)$	22.3	22.3	22.3	7.84	36.76	22.3	22.3	22.3	22.3	22.3	22.3	22.3	22.3
Θ (mV)	20	20	20	20	20	16	24	20	20	20	20	20	20
$\kappa\ (m)$	10^{-4}	10^{-4}	10^{-4}	10^{-4}	10^{-4}	10^{-4}	10^{-4}	10^{-5}	10^{-3}	10^{-4}	10^{-4}	10^{-4}	10^{-4}
$T\ (K)$	293	293	293	293	293	293	293	293	293	264	322	293	293
Re_λ	51	51	51	51	51	51	51	51	51	51	51	29	120

Simulation 0 represents a base case, with A and B variations corresponding to the modification of each considered parameter, either higher or lower than that of the base value.

A typical interaction for the base case is presented in Figure 12 where a bouncing event is presented, the middle plot of which demonstrates the surrounding fluid field at the point of impact between two particles. On the left we observe the evolution of the relative distance between the particles, which reduces up until the point of impact and starts to slow at small separation distances, likely due to the particles entering the effective range of the DLVO forces. Despite this, the particles continue to move closer and bounce off one another. The plot on the right shows the time evolution of their relative velocity, which exhibits much more chaotic behaviour as the various forces act on the particles. In the region before $t = 5\ s$, the velocity profile exhibits a consistent magnitude and rms. As the particles draw closer after this point, the relative velocity increases due to the van der

Waals attraction until the point of impact where it begins to reduce again rapidly as energy is dispersed in the collision. After the collision, the particles once again separate, leading to similar behaviour as seen at the start of the interaction.

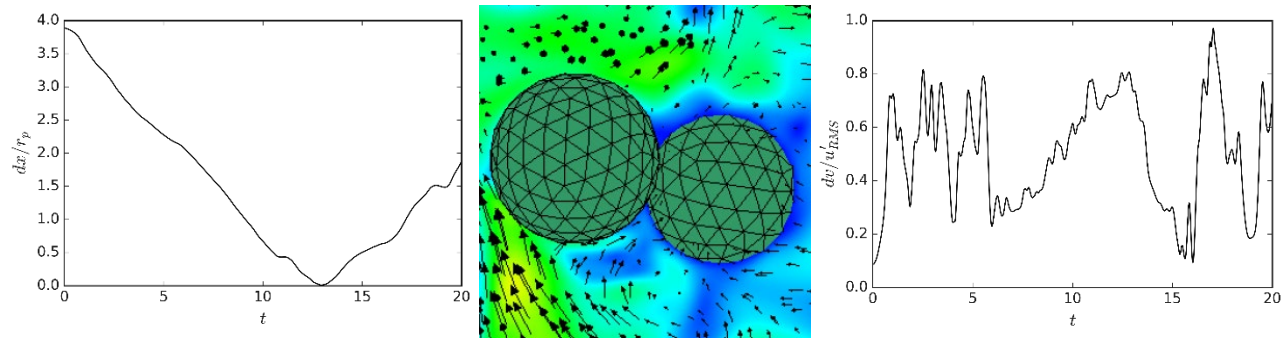

Figure 12: Pseudocolour and velocity vector representation of binary particle interaction at point of impact during collision event for the base case (middle). Surrounding plots demonstrate the time (in s) evolution of interparticle distance (left) and the relative particle velocity (right).

The first parameter for consideration is the normal coefficient of restitution, e_n, which can be manipulated by a variety of means. These include coating the particles with viscous films (Liu et al., 2016), injecting a secondary solid phase which will adsorb onto the surface of the particles, or using other behavioural modification techniques to increase the size and density of the particulate structures. Figure 13 demonstrates the sensitivity of particle interaction events to the restitution coefficient by considering the mean relative intersurfacial distance and mean relative velocity between the two particles. To obtain these distributions, the intersurfacial separation distance, $dx = \left|x_{P,2} - x_{P,1}\right| - 2r_p$, and the relative velocity, $dv = \left|u_{P,2} - u_{P,1}\right|$, were measured from the point of injection at equal intervals of 100 timesteps across the period $0 \leq t \leq 20$ which was sufficient time in all three boxes for the system to exhibit interaction dynamics (either agglomeration, bouncing or missing, and turbulent motion). After each interaction, the simulation was reset with a new random injection point somewhere within the domain. Statistics were obtained over at least 40 instances of one typical interaction setup, with total sample numbers for each system chosen to ensure smooth resulting PDFs. Clearly this property has a strong effect on collision dynamics. A high coefficient of normal restitution means that particles tend to spend less time close to each other throughout the event. This is likely due to their retention of kinetic energy upon impact, allowing them to overcome the van der Waals attraction force, which causes them to return to a region where turbulence dominates. The right-hand plot in Figure 13 indicates a larger spread of relative velocities for increases in the coefficient of restitution, suggesting a greater variety of interaction events where particles frequently change their velocity. At lower coefficients of restitution, particles undergoing collisions are less likely to reach their greater pre-collision velocities and so the distribution is shifted towards zero. Zero values of the intersurfacial distance indicating touching particles also increase significantly as the coefficient of restitution decreases, with the highest value of this parameter reducing

particle contact to close to zero over the interactions considered. It should be noted that zero values of this quantity do not necessarily imply agglomeration, as some particles will also bounce off one another following impact.

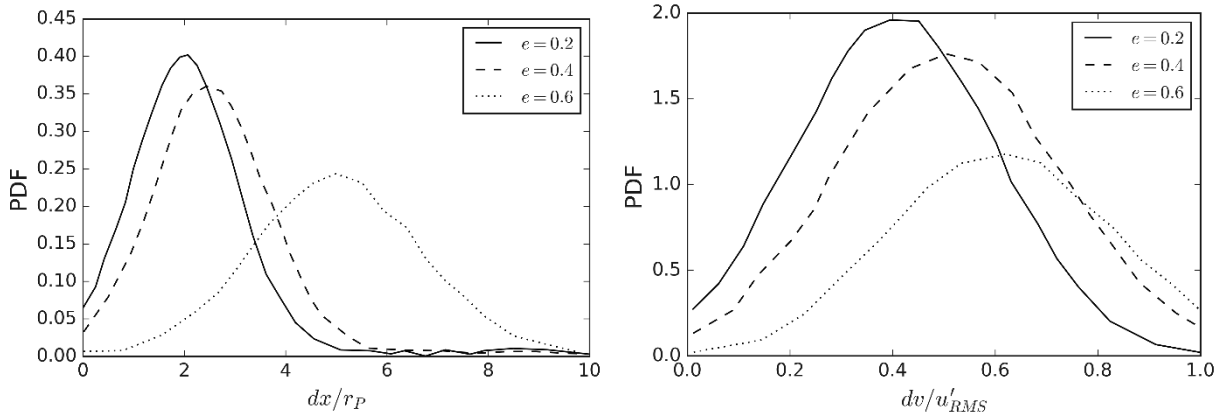

Figure 13: Effect of variation of coefficient of restitution on mean relative intersurfacial distance and mean relative velocity for binary particle interactions sampled over at least 40 instances.

The Hamaker constant directly modulates the attraction term in the DLVO potential equation, and in previous studies (Njobuenwu and Fairweather, 2017) has been shown to influence the agglomeration rate. In Figure 14 we observe that actually the Hamaker constant has little effect on the resulting probability density function of relative displacement. This implies that, for the range of values studied, the amount of time particles spend close to each other is actually independent of the force of the attraction. Consideration of the outcomes of the interactions shows that in all cases, some particles undergo near hits but then travel past each other, advected away by turbulence once they overshoot the attractive region. This would make the agglomeration mechanism less sensitive to the Hamaker constant, since any agglomeration would only depend on the velocity vectors of the particles at the start of the interaction event. The above explanation is reflected in the plot of relative velocity. Despite the particles not spending significantly different amounts of time close to each other, they differ quite extensively in their relative velocity, with a high Hamaker constant showing that the particles travel faster and over a greater range of speeds. If the particles are travelling past each other and not colliding then this would be the case since the acceleration and subsequent range of relative velocities would depend primarily on the attraction strength. This behaviour implies that in high concentration fluid-particle dispersions, the Hamaker constant would also influence decoupling the particles from local flow velocities, particularly for inertial particles. For low Stokes number particles, or tracers, the forces may cause additional collisions since the attractive forces may cause particle motion to deviate away from the fluid flow streamlines, which could lead to increased agglomeration rates, particularly in the bulk flow region. In practice, the Hamaker constant has been shown to be adjustable by adding salt to the fluid (Shahidzadeh et al., 1998) and has also been shown to be temperature dependent (Bergström, 1997). By tuning this parameter, control is obtained surrounding the impact velocity of colliding particles.

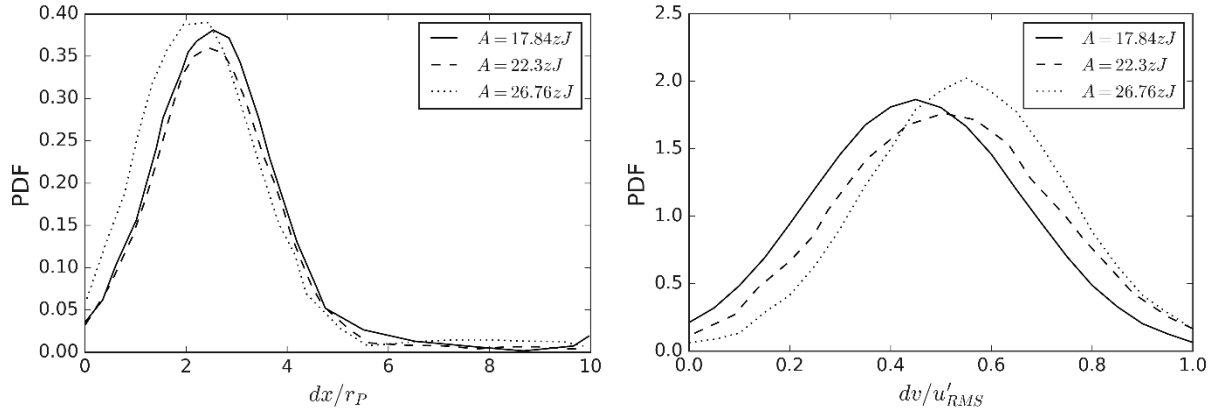

Figure 14: Effect of variation of Hamaker constant on mean relative intersurfacial distance and mean relative velocity for binary particle interactions sampled over at least 40 instances.

Figure 15 illustrates the sensitivity of the relative displacement and relative velocity to surface potential, which linearly modulates the strength of the electric double layer repulsion. In both plots, it is evident that for the range of parameters considered, there is little effect on the resulting interaction dynamics. This is due to the very short range associated with this force particularly with the chosen Debye length. As the particles reach low separation distances, the force is not strong enough to overcome the van der Waals attraction. That said, it is likely that this parameter would have a much more pronounced effect on particle-scale motion of much smaller particles.

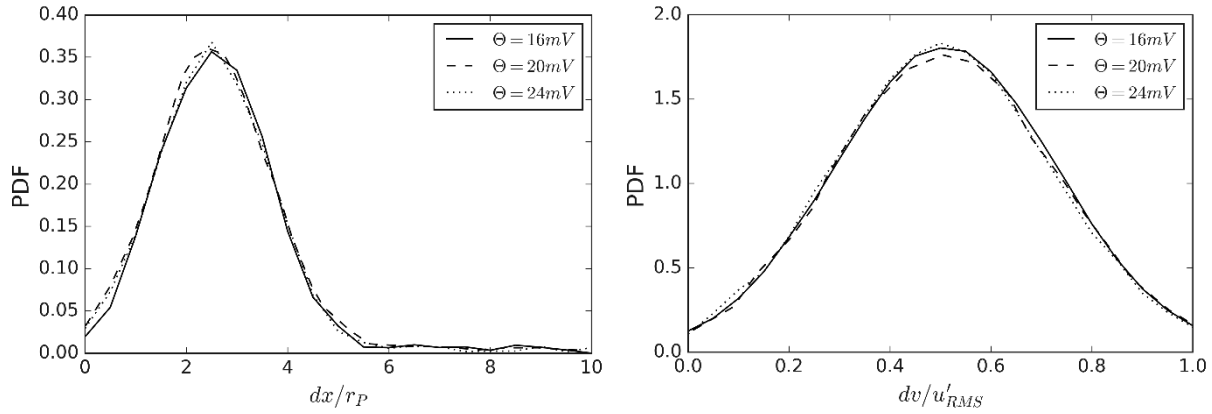

Figure 15: Effect of variation of reduced surface potential on mean relative intersurfacial distance and mean relative velocity for binary particle interactions sampled over at least 40 instances.

The effect of manipulation of the inverse Debye length is presented in Figure 16. From these results, it is evident that at low inverse Debye lengths, the mean relative displacement is largely unchanged from that of the standard case. Similar observations are made for the mean relative velocity with perhaps a slight overall increase. In increasing the inverse Debye length by an order of magnitude from the base case, the range of relative displacements, as well as the mean, is increased greatly. In distributing the electric double layer force over a much greater distance, the repulsion may dominate in regions

where the van der Waals attraction is still weak. Considering the distribution of relative velocities, these are lowered, likely due to the repulsion slowing the particles down as they approach each other. By tuning the salt concentration in such systems, hence manipulating the ionic strength, the Debye screening length is capable of being increased or reduced (Kontogeorgis et al., 2018).

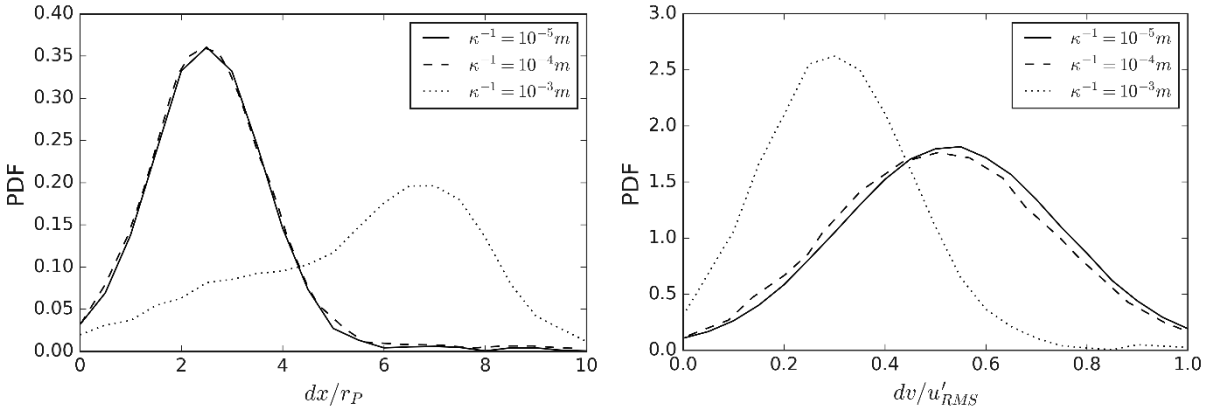

Figure 16: Effect of variation of inverse Debye length on mean relative intersurfacial distance and mean relative velocity for binary particle interactions sampled over at least 40 instances.

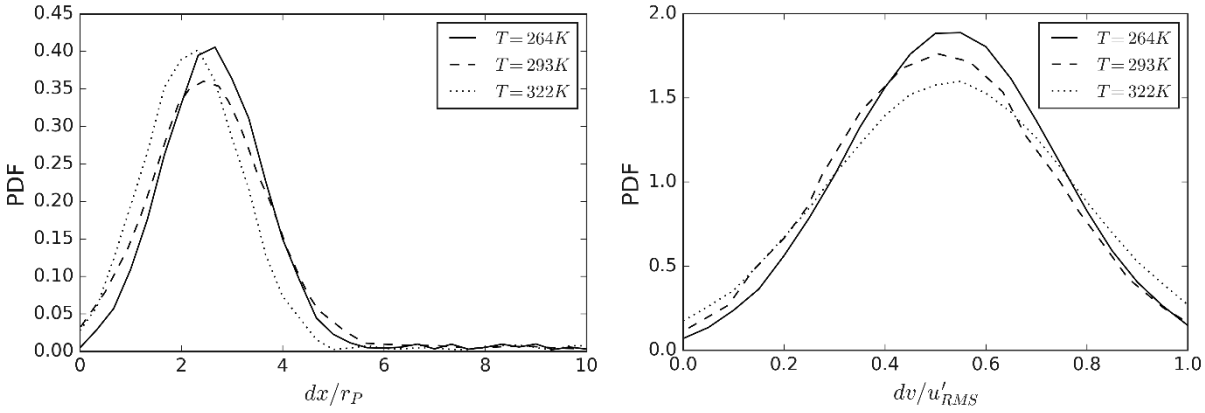

Figure 17: Effect of variation of temperature on mean relative intersurfacial distance and mean relative velocity for binary particle interactions sampled over at least 40 instances.

The effect of modification of temperature is presented in Figure 17. This parameter modulates the electric double layer linearly, and to isolate this modulation, variations of other parameters with temperature are not considered here. That said, over the range of temperatures considered (which is very broad and beyond any range likely to be encountered in practice), very little effect on the resulting collision behaviour is observed. In the plot of intersurfacial displacement, an increase in temperature slightly reduces the mean distance particles spend close to each other, and slightly increases the range of relative velocities. That said, the DNS simulation did not solve for the temperature field, the addition of which may have further implications for

both the turbulence field and the particle-turbulence energy transfer during collisions such as these which may yield different behaviour.

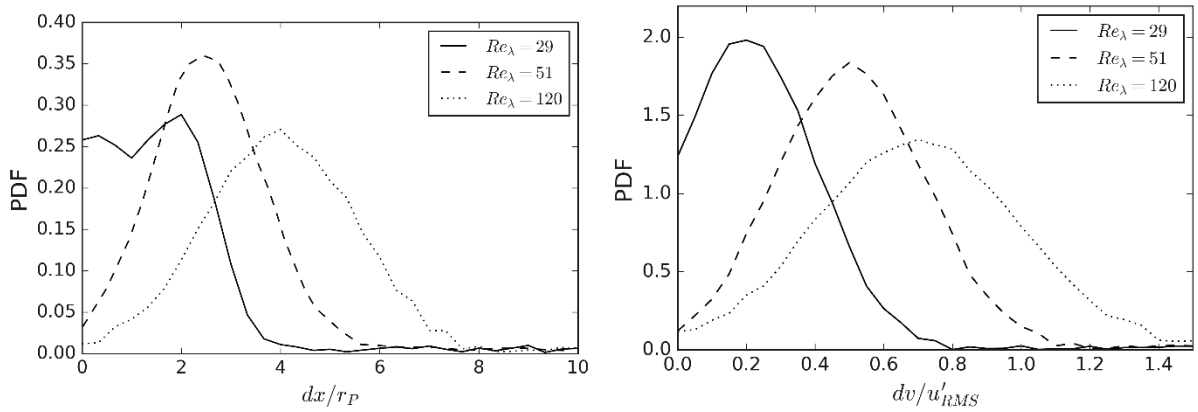

Figure 18: Effect of variation of Reynolds number based on the Taylor microscale on mean relative intersurfacial distance and mean relative velocity for binary particle interactions sampled over at least 40 instances.

Finally, the effect of variation of Reynolds number was studied by performing the binary particle interactions in the three isotropic boxes outlined in Section III-B. In decreasing the Reynolds number from the base case value, shown in Figure 15, the particles spend more time in close proximity to each other, with the effects of the collision dominating their motion. Their range of velocities is also lowered, with many instances of particles moving with the same velocity indicating an agglomeration event. Upon increasing the Reynolds number, it seems that agglomeration is actually deterred, with the increased turbulence either removing particles from their impact trajectories or carrying them away after a collision takes place in which they do not lose enough kinetic energy and overcome the close range attraction. Similarly, the range of velocities is increased, with many particles obtaining much higher velocities than they were injected with. Given a collision is about to occur, the turbulence increase hence reduces the chance that the collision will result in an agglomeration event, which has been observed in previous LPT studies (Njobuenwu and Fairweather, 2017; Mortimer et al., 2020).

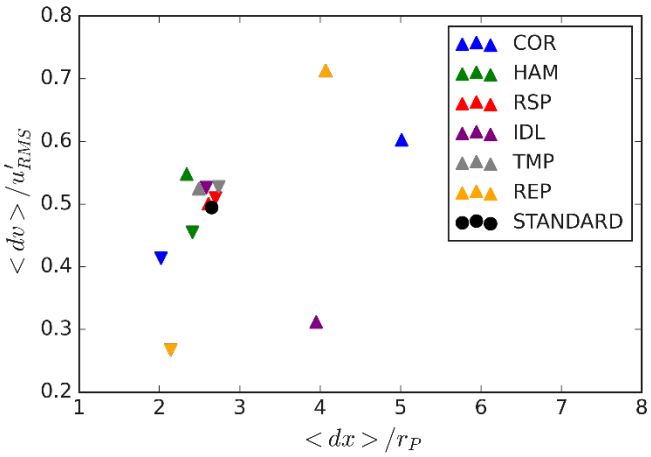

Figure 19: Effect of behavioural modification parameters on the mean interparticle distance and the mean relative velocity during an interaction event. Up and down arrows indicate increase and decrease in parameter, respectively, whilst fixing all other parameters.

The results of the behavioural modification effects considered in this study are summarized in Figure 19, which illustrates the impact of increasing or decreasing a certain parameter on the mean interparticle distance and mean relative velocity parameter space. It can be identified from this plot that both Reynolds number (REP) and coefficient of restitution (COR) exhibit the strongest modification effects, which both increase relative distance and velocity as each of these parameters is increased. Here, the increase has a larger impact on the relative distance for the coefficient of restitution, and similarly the relative velocity is impacted more by the turbulence intensity. Conversely, an opposite trend is observed for increasing inverse Debye length (IDL), where the relative velocity is reduced as separation distance increases. Note that reducing the inverse Debye length has little effect, as the distance over which the electric double layer is effective reduces to scales lower than those considered in the simulation. The remaining parameters (HAM – Hamaker constant, RSP – reduced surface potential, TMP – temperature) show limited response for the range of values considered, and in future studies a larger range of values should be investigated. Note that the 'standard' point in Figure 18 refers to values for no behavioral modification effect.

IV. CONCLUSIONS

In order to simulate and study binary particle interactions, and to assess behavioural modification techniques for turbulent multiphase flows, this work described a particle-resolved immersed boundary method which was implemented into the spectral element-based DNS code, Nek5000. The ghost-cell mirroring method was used to ensure the no-slip condition on the particle surface is met and, for the first time, both hard-sphere collisions and interparticle DLVO forces were included in the calculations. A validation of the IB method was performed which considers calculation of the drag coefficient on a stationary spherical particle subject to flow fields with differing particle Reynolds numbers. The results showed very strong agreement across the range of Reynolds numbers studied, with very slight inaccuracies at Reynolds numbers greater than 100. Periodic

boxes of isotropic turbulence at three different Reynolds numbers based on the Taylor microscale were generated using the linear forcing method, with turbulence levels representative of various regions present in a $Re_\tau = 180$ turbulent channel flow. The transition from initial conditions to steady state isotropic turbulence within these boxes was demonstrated with temporal plots of the mean of the velocity fluctuation throughout the box. From these, a statistically stationary state was identified, with mean flow quantities negligible compared to the root-mean-square of the velocity fluctuations. Slices of velocity magnitude contour plots were also presented for all levels of turbulence, with each possessing their own characteristic eddy length spectra and range of velocities.

By combining the implemented IB method within the boxes of homogeneous isotropic turbulence, structure-resolved particle-particle interactions were simulated. Particles were injected with initial conditions matching those present in pre-collision events sampled from a four-way coupled turbulent channel flow performed with identical dispersed, but point, particles at $Re_\tau = 180$. These simulations were used to study the effect of varying certain mechanical and chemical parameters on particle collision and aggregation dynamics. We observe that increasing the coefficient of restitution discourages low particle separation distances, as particles do not lose enough energy on collision to be overcome by the van der Waals attractive force. This also causes a greater spread in particle velocity, as the particles are separated and reintroduced into regions where turbulence dominates. It is shown that increasing the Hamaker constant increases the mean velocity of the interacting particles, but its effect on the probability of collision and possible agglomeration is very low since the distribution of separation distances is unchanged. It is likely that in this case, particles are attracted to each other but sometimes do not collide, leading to their reintroduction into regions of turbulence where DLVO forces are uninfluential. Varying the electric double layer surface charge had little effect on the resulting interaction statistics. It is noted that the effective range for this force is very low and the variation considered herein was too low for modifications to be influential on the resulting particle behaviour. The inverse Debye length showed little effect when decreasing it from the chosen base case value, but exhibited a strong effect when increasing it by an order of magnitude, such that it increased the mean interparticle distance by a factor of two, and greatly increased the range of interparticle distances, discouraging collision events where the particles remain close to each other. Additionally, the velocity spread was reduced, meaning that electric double layer repulsion not only plays a part in repelling the particles, but removes energy from them as well. Variation of temperature only yielded very slight differences in interaction dynamics, with higher temperatures discouraging particles from colliding and potentially agglomerating, and reducing the variation of relative velocities. Finally, at increased Reynolds numbers based on the Taylor microscale, the particles were less likely to spend time close to each other, with the effects of the hydrodynamic forces overcoming the DLVO forces at low separation distances.

The results presented herein not only demonstrate the capabilities of the structure-resolved model, but also indicate possible parameters which can be employed to encourage or discourage particle collisions and potential agglomeration. Of most note are the coefficient of restitution, the inverse Debye length (related to ionic strength) and turbulence level, all three of which have associated real-world modifications which can be used to implement the required changes. For instance, coating particles, adding salt to the flow and modifying the flow rate will allow each of these parameters to be modified, respectively. With this knowledge, further work should include determining the impact of these key parameters in bulk-scale flows, where the turbulence dynamics leading up to the collision are also captured.

V. ACKNOWLEDGEMENTS

The authors are grateful for funding from the UK Engineering and Physical Sciences Research Council through the TRANSCEND (Transformative Science and Engineering for Nuclear Decommissioning) project (EP/S01019X/1).

VI. DATA AVAILABILITY

The data that support the findings of this study are available from the corresponding author upon reasonable request.

REFERENCES

M. N. Ardekani, P. Costa, W. P. Breugem and L. Brandt. "Numerical study of the sedimentation of spheroidal particles." *International Journal of Multiphase Flow.* **87**, 16-34. (2016).

S. Balachandar and J. Eaton. "Turbulent Dispersed Multiphase Flow." *Annual Review of Fluid Mechanics.* **42**, 111-133. (2010).

L. Bergström. "Hamaker constants of inorganic materials." *Advances in Colloid and Interface Science.* **70**, 125-169. (1997).

R. P. Beyer and R. J. LeVeque. "Analysis of a one-dimensional model for the immersed boundary method." *SIAM Journal on Numerical Analysis.* **29**, 332-364. (1992).

K. A. Buist, L. Seelen, N. Deen, J. Padding and J. Kuipers. "On an efficient hybrid soft and hard sphere collision integration scheme for DEM." *Chemical Engineering Science.* **153**, 363-373. (2016).

C. Chi, B. J. Lee and H. G. Im. "An improved ghost-cell immersed boundary method for compressible flow simulations." *International Journal for Numerical Methods in Fluids.* **83**, 132-148. (2017).

P. Costa, B. J. Boersma, J. Westerweel and W.-P. Breugem. "Collision model for fully resolved simulations of flows laden with finite-size particles." *Physical Review E.* **92**, 053012. (2015).

C. Crowe, R. Gore and T. Troutt. "Particle dispersion by coherent structures in free shear flows." *Particulate Science and Technology.* **3**, 149-158. (1985).

T. Dbouk and D. Drikakis. "On coughing and airborne droplet transmission to humans." *Physics of Fluids.* **32**, 053310. (2020).

B. Derjaguin and L. Landau. "Theory of the stability of strongly charged lyophobic sols and of the adhesion of strongly charged particles in solutions of electrolytes." *Acta Physicochim. URSS.* **14**, 633-662. (1941).

J. J. Derksen. "Simulations of granular bed erosion due to laminar shear flow near the critical Shields number." *Physics of Fluids.* **23**, 113303. (2011).

T. Dombre, U. Frisch, M. Henon, J. M. Greene and A. M. Soward. "Chaotic streamlines in the ABC flows." *Journal of Fluid Mechanics.* **167**, 353. (1986).

J. K. Eaton. "Two-way coupled turbulence simulations of gas-particle flows using point-particle tracking." *International Journal of Multiphase Flow.* **35**, 792-800. (2009).

J. K. Eaton and J. Fessler. "Preferential concentration of particles by turbulence." *International Journal of Multiphase Flow.* **20**, 169-209. (1994).

S. Elghobashi and G. C. Truesdell. "Direct simulation of particle dispersion in a decaying isotropic turbulence." *Journal of Fluid Mechanics.* **242**, 655-700. (2006).

M. Fairweather and J. Yao. "Mechanisms of particle dispersion in a turbulent, square duct flow." *AIChE journal.* **55**, 1667-1679. (2009).

J. R. Fessler, J. D. Kulick and J. K. Eaton. "Preferential concentration of heavy particles in a turbulent channel flow." *Physics of Fluids.* **6**, 3742-3749. (1994).

P. F. Fischer, J. W. Lottes and S. G. Kerkemeier. 2008. *Nek5000.* [Online]. [Accessed 1st September]. Available from: http://nek5000.mcs.anl.gov

D. Goldstein, R. Handler and L. Sirovich. "Modeling a No-Slip Flow Boundary with an External Force Field." *Journal of Computational Physics.* **105**, 354-366. (1993).

P. Gondret, M. Lance and L. Petit. "Bouncing motion of spherical particles in fluids." **14**, 643-652. (2002).

M. Hosaka, T. Nagata, S. Takahashi and K. Fukuda. "Numerical simulation on solid–liquid multiphase flow including complex-shaped objects with collision and adhesion effects using immersed boundary method." *Multiphase Flow Theory Appl.* **6**, 162-175. (2018).

H. H. Hu. "Direct simulation of flows of solid-liquid mixtures." *International Journal of Multiphase Flow.* **22**, 335-352. (1996).

H. H. Hu, N. A. Patankar and M. Zhu. "Direct numerical simulations of fluid–solid systems using the arbitrary Lagrangian–Eulerian technique." *Journal of Computational Physics.* **169**, 427-462. (2001).

A. Hussain, J. Jeong and J. Kim. "Structure of turbulent shear flows." (1987).

R. Jain, S. Tschisgale and J. Fröhlich. "A collision model for DNS with ellipsoidal particles in viscous fluid." *International Journal of Multiphase Flow.* **120**, 103087. (2019).

J. Janin, F. Duval, C. Friess and P. Sagaut. "A new linear forcing method for isotropic turbulence with controlled integral length scale." **33**, 045127. (2021).

M. H. Kasbaoui, D. L. Koch and O. Desjardins. "The rapid distortion of two-way coupled particle-laden turbulence." *Journal of Fluid Mechanics.* **877**, 82-104. (2019).

W. Kim and H. Choi. "Immersed boundary methods for fluid-structure interaction: A review." *International Journal of Heat and Fluid Flow.* **75**, 301-309. (2019).

Y. Kim and C. S. Peskin. "Penalty immersed boundary method for an elastic boundary with mass." *Physics of Fluids.* **19**, 053103. (2007).

G. M. Kontogeorgis, B. Maribo-Mogensen and K. Thomsen. "The Debye-Hückel theory and its importance in modeling electrolyte solutions." *Fluid Phase Equilibria.* **462**, 130-152. (2018).

A. Li and G. Ahmadi. "Dispersion and deposition of spherical particles from point sources in a turbulent channel flow." *Aerosol Science and Technology.* **16**, 209-226. (1992).

H. Li, X. Ku and J. Lin. "Eulerian–Lagrangian simulation of inertial migration of particles in circular Couette flow." **32**, 073308. (2020).

Q. Li, J. Song, C. Li, Y. Wei and J. Chen. "Numerical and experimental study of particle deposition on inner wall of 180° bend." *Powder Technology.* **237**, 241-254. (2013).

G. Liu, F. Yu, H. Lu, S. Wang, P. Liao and Z. Hao. "CFD-DEM simulation of liquid-solid fluidized bed with dynamic restitution coefficient." *Powder Technology.* **304**, 186-197. (2016).

F. Lucci, A. Ferrante and S. Elghobashi. "Modulation of isotropic turbulence by particles of Taylor length-scale size." *Journal of Fluid Mechanics.* **650**, 5-55. (2010).

J. L. Lumley. "Drag reduction in turbulent flow by polymer additives." *J Polym Sci, Part D, Macromol Rev.* **7**, 263-290. (1973).

T. Lundgren. 2003. *Linearly Forces Isotropic Turbulence.* Minnesota University Minneapolis.

H. Luo, B. Yin, H. Dai and J. Doyle. "A 3D computational study of the flow-structure interaction in flapping flight." In: *48th AIAA aerospace sciences meeting including the new horizons forum and aerospace exposition*, 556. (2010).

J. G. M. Kuerten. "Point-Particle DNS and LES of Particle-Laden Turbulent flow - a state-of-the-art review." *Flow, Turbulence and Combustion.* **97**, 689-713. (2016).

A. Mark and B. G. van Wachem. "Derivation and validation of a novel implicit second-order accurate immersed boundary method." *Journal of Computational Physics.* **227**, 6660-6680. (2008).

M. Maxey. "The motion of small spherical particles in a cellular flow field." *The Physics of Fluids.* **30**, 1915-1928. (1987).

M. R. Maxey and J. J. Riley. "Equation of motion for a small rigid sphere in a nonuniform flow." *Physics of Fluids.* **26**, 883-889. (1983).

Y. Mizuno, S. Takahashi, K. Fukuda and S. Obayashi. "Direct numerical simulation of gas–particle flows with particle–wall collisions using the immersed boundary method." *Applied Sciences.* **8**, 2387. (2018).

J. Mohd-Yusof. "Combined immersed-boundary/B-spline methods for simulations of flow in complex geometries." *Center for turbulence research annual research briefs.* **161**, 317-327. (1997).

R. Monchaux and A. Dejoan. "Settling velocity and preferential concentration of heavy particles under two-way coupling effects in homogeneous turbulence." *Physical Review Fluids.* **2**, 104302. (2017).

P. Mortensen, H. Andersson, J. Gillissen and B. Boersma. "Dynamics of prolate ellipsoidal particles in a turbulent channel flow." *Physics of Fluids.* **20**, 093302. (2008).

L. Mortimer and M. Fairweather. "Density ratio effects on the topology of coherent turbulent structures in two-way coupled particle-laden channel flows." *Physics of Fluids.* **32**, 103302. (2020).

L. F. Mortimer, D. O. Njobuenwu and M. Fairweather. "Near-wall dynamics of inertial particles in dilute turbulent channel flows." *Physics of Fluids.* **31**, 063302. (2019).

L. F. Mortimer, D. O. Njobuenwu and M. Fairweather. "Agglomeration dynamics in liquid–solid particle-laden turbulent channel flows using an energy-based deterministic approach." *Physics of Fluids.* **32**, 043301. (2020).

R. Nieto and L. Gimeno. "A database of optimal integration times for Lagrangian studies of atmospheric moisture sources and sinks." *Scientific data.* **6**, 1-10. (2019).

D. O. Njobuenwu and M. Fairweather. "Simulation of deterministic energy-balance particle agglomeration in turbulent liquid-solid flows." *Physics of Fluids.* **29**, 083301. (2017).

B. Oesterle and A. Petitjean. "Simulation of particle-to-particle interactions in gas solid flows." *International Journal of Multiphase Flow.* **19**, 199-211. (1993).

R. Ouchene. "Numerical simulation and modeling of the hydrodynamic forces and torque acting on individual oblate spheroids." **32**, 073303. (2020).

C. S. Peskin. "Numerical analysis of blood flow in the heart." *Journal of Computational Physics.* **25**, 220-252. (1977).

C. S. Peskin. "The immersed boundary method." *Acta numerica.* **11**, 479-517. (2002).

U. Piomelli, P. Moin and J. H. Ferziger. "Model consistency in large eddy simulation of turbulent channel flows." *The Physics of fluids.* **31**, 1884-1891. (1988).

S. B. Pope. 2001. *Turbulent flows*. IOP Publishing.

C. Rosales and C. Meneveau. "Linear forcing in numerical simulations of isotropic turbulence: Physical space implementations and convergence properties." *Physics of Fluids.* **17**, 095106. (2005).

F. Rousta and B. Lessani. "Direct numerical simulation of turbulent particle-laden flows: effects of Prandtl and Stokes numbers." *International Journal of Heat and Mass Transfer.* 120724. (2020).

A. Segalini, R. Örlü, P. Schlatter, P. H. Alfredsson, J.-D. Rüedi and A. J. E. i. f. Talamelli. "A method to estimate turbulence intensity and transverse Taylor microscale in turbulent flows from spatially averaged hot-wire data." **51**, 693-700. (2011).

N. Shahidzadeh, D. Bonn, K. Ragil, D. Broseta and J. Meunier. "Sequence of Two Wetting Transitions Induced by Tuning the Hamaker Constant." *Physical Review Letters.* **80**, 3992-3995. (1998).

A. L. F. Silva, A. R. d. Silva and A. d. Silveira Neto. "Numerical simulation of two-dimensional complex flows around bluff bodies using the immersed boundary method." *Journal of the Brazilian Society of Mechanical Sciences and Engineering.* **29**, 379-387. (2007).

A. Soldati and C. Marchioli. "Physics and modelling of turbulent particle deposition and entrainment: Review of a systematic study." *International Journal of Multiphase Flow.* **35**, 827-839. (2009).

J. Stenhammar, P. Linse, H. Wennerström and G. Karlström. "An Exact Calculation of the van der Waals Interaction between Two Spheres of Classical Dipolar Fluid." *The Journal of Physical Chemistry B.* **114**, 13372-13380. (2010).

G. G. Stokes. 1851. *On the effect of the internal friction of fluids on the motion of pendulums.* Pitt Press Cambridge.

R. Sungkorn and J. J. Derksen. "Simulations of dilute sedimenting suspensions at finite-particle Reynolds numbers." **24**, 123303. (2012).

Y.-H. Tseng and J. H. Ferziger. "A ghost-cell immersed boundary method for flow in complex geometry." *Journal of Computational Physics.* **192**, 593-623. (2003).

M. Uhlmann. "An immersed boundary method with direct forcing for the simulation of particulate flows." *Journal of Computational Physics.* **209**, 448-476. (2005).

E. J. W. Verwey and J. T. G. Overbeek. "Theory of the stability of lyophobic colloids." *Journal of Colloid Science.* **10**, 224-225. (1955).

A. Vreman. "Particle-resolved direct numerical simulation of homogeneous isotropic turbulence modified by small fixed spheres." *Journal of Fluid Mechanics.* **796**, 40-85. (2016).

A. W. Vreman and J. G. M. Kuerten. "Comparison of direct numerical simulation databases of turbulent channel flow at Re-tau=180." *Physics of Fluids.* **26**, (2014).

D. K. Walters and W. H. Luke. "Computational Fluid Dynamics Simulations of Particle Deposition in Large-Scale, Multigenerational Lung Models." *Journal of Biomechanical Engineering.* **133**, 011003-011003-011008. (2010).

D. Wang, B. Chang, T. Zhang, S. Tan and F. Niu. "Evaluation of chemical effects on fuel assembly blockage following a loss of coolant accident in nuclear power plants." *International Journal of Energy Research.* **44**, 5488-5499. (2020).

T. Wei and W. Willmarth. "Modifying turbulent structure with drag-reducing polymer additives in turbulent channel flows." *Journal of Fluid Mechanics.* **245**, 619-641. (1992).

C. Winkler, S. L. Rani and S. Vanka. "A numerical study of particle wall-deposition in a turbulent square duct flow." *Powder Technology.* **170**, 12-25. (2006).

WMSYM. 2016. *Sellafield Additional Sludge Retrievals, A Significant Step in Decommissioning Part of the U.K.'s Nuclear Legacy.* WMSYM.

J. Yang and E. Balaras. "An embedded-boundary formulation for large-eddy simulation of turbulent flows interacting with moving boundaries." *Journal of Computational Physics.* **215**, 12-40. (2006).

M. Zastawny, B. Wachem and J. Oliveira. 2010. *An Immersed Boundary Method for Interacting Particles.*

H. Zhang, F. X. Trias, A. Gorobets, A. Oliva, D. Yang, Y. Tan and Y. Sheng. "Effect of collisions on the particle behavior in a turbulent square duct flow." *Powder Technology.* **269**, 320-336. (2015).

X. Zhang, M. Luo, E. Wang, L. Zheng and C. Shu. "Numerical simulation of magnetic nano drug targeting to atherosclerosis: Effect of plaque morphology (stenosis degree and shoulder length)." *Computer Methods and Programs in Biomedicine.* **195**, 105556. (2020).

F. Zhao, W. George and B. Van Wachem. "Four-way coupled simulations of small particles in turbulent channel flow: The effects of particle shape and Stokes number." *Physics of Fluids.* **27**, 083301. (2015).

L. Zhao, C. Marchioli and H. Andersson. "Stokes number effects on particle slip velocity in wall-bounded turbulence and implications for dispersion models." *Physics of Fluids.* **24**, 021705. (2012).